Electrochimica Acta 411 (2022) 140038

Contents lists available at ScienceDirect

Electrochimica Acta

journal homepage: www.journals.elsevier.com/electrochimica-acta

Crosslinked poly(acrylic acid) enhances adhesion and electrochemical performance of Si anodes in Li-ion batteries

Jiarong He [a,b,*], Chittaranjan Das [a], Fan Yang [b], Julia Maibach [a]

[a] Institute for Applied Materials (IAM), Karlsruhe Institute of Technology (KIT), Hermann-von-Helmholtz-Platz 1, 76344 Eggenstein-Leopoldshafen, Germany
[b] School of Materials and Energy, Guangdong University of Technology, Guangzhou 510006, China

ARTICLE INFO

Keywords:
Water-soluble Binders
Si Anode
Crosslinked Poly (acrylic acid)
Pentaerythritol
3D Interconnected Network

ABSTRACT

Water-soluble binders such as poly (acrylic acid) (PAA) possess many advantages in the slurry and electrode preparation due to their low-cost and environmental friendliness. However, due to the linear nature of these binders, they are susceptible to slide under the continuous volume variation of Si-containing anodes during cycling. Therefore, a three-dimensional (3D) interconnected polymeric network is required to provide robust mechanical adhesion with the Si particles to maintain the electrode integrity for excellent cycle stability. Here, pentaerythritol (PER) is used as a crosslinking agent to connect the linear PAA binder to enhance its adhesion strength for Si anodes, which is systematically confirmed using Fourier-transform infrared spectroscopy (FT-IR), X-ray photoelectron spectroscopy (XPS) and thermogravimetric (TG) measurements. Si electrodes with crosslinked PAA-PER binder show enhanced adhesion and elasticity, exhibiting a more robust electrode integrity than purely PAA-based Si electrodes. Galvanostatic cycling shows that Si-PAA-5%PER electrodes maintain a higher discharge capacity of 514.3 mAh g^{-1} (after 10 cycles) for micro-sized and 1502.1 mAh g^{-1} (after 105 cycles) for nano-sized Si particles compared to 257.6 mAh g^{-1} and 1413.9 mAh g^{-1} for micro- and nano-sized Si in Si-PAA electrodes, respectively. XPS analyses on cycled electrodes confirmed that crosslinked PAA-PER binder has no negative effects on the SEI formation and its functionality in Si electrodes. SEM cross-sections reveal that Si-PAA-5%PER electrodes show reduced electrode thickness variation (micro-/nano-: 114.2%/182.2%) than that of Si-PAA electrodes (micro-/nano-: 134.1%/212.0%) after cycling, which indicates that crosslinked PAA-PER binder can enhance the electrode integrity due to its 3D interconnected network. This work provides meaningful insight into the exploration of novel binders and their impact on the SEI formation and functionality, especially for high-capacity alloy-type anode materials.

1. Introduction

High energy density and stable cycle performance in advanced lithium-ion batteries (LIBs) are required for devices relying on electrochemical energy storage such as consumer electronics and electric vehicles [1]. Graphite, the traditional anode material (372 mA h g^{-1} for LiC_6), has been widely applied in commercial LIBs due to its excellent cycle stability [2]. However, the low theoretical capacity (372 mAh g^{-1}) prompts more research efforts to explore alternative anode materials, such as alloy-type materials. Silicon (Si), one of the most promising alloying type anode candidates, has been widely studied in recent years due to its high theoretical specific capacity ($Li_{4.4}Si$, 4200 mAh g^{-1}) and low discharge potential. However, Si anodes suffer fast capacity decay from internal stress induced by the large volume variations (up to 300%) during cycling, accompanied with the loss of electrical contact, excess formation of solid-electrolyte interphase (SEI) on newly exposed Si surface and even delamination of the Si active material from the current collector [3].

To alleviate the above issues, research efforts have focused on addressing the fast degradation of Si anodes in several ways: i) nano morphology design of Si materials (e.g. nanoparticles [4], nanowires [5] and porous/hollow nanostructure [6, 7]); ii) fabrication of Si/C composite materials by coating and embedding Si particles in a conductive matrix (amorphous carbon [8], carbon nanotubes [9] and graphene [10], etc.); iii) exploration of novel multifunctional polymeric binders (self-healing recovery [11] and three-dimensional interconnected network [12], etc.). Particularly, multifunctional binders have gained considerable attention since the structural integrity of Si electrodes and

* Corresponding author.
E-mail addresses: jiarong.he@gdut.edu.cn (J. He), julia.maibach@kit.edu (J. Maibach).

https://doi.org/10.1016/j.electacta.2022.140038
Received 10 December 2021; Received in revised form 19 January 2022; Accepted 6 February 2022
Available online 7 February 2022

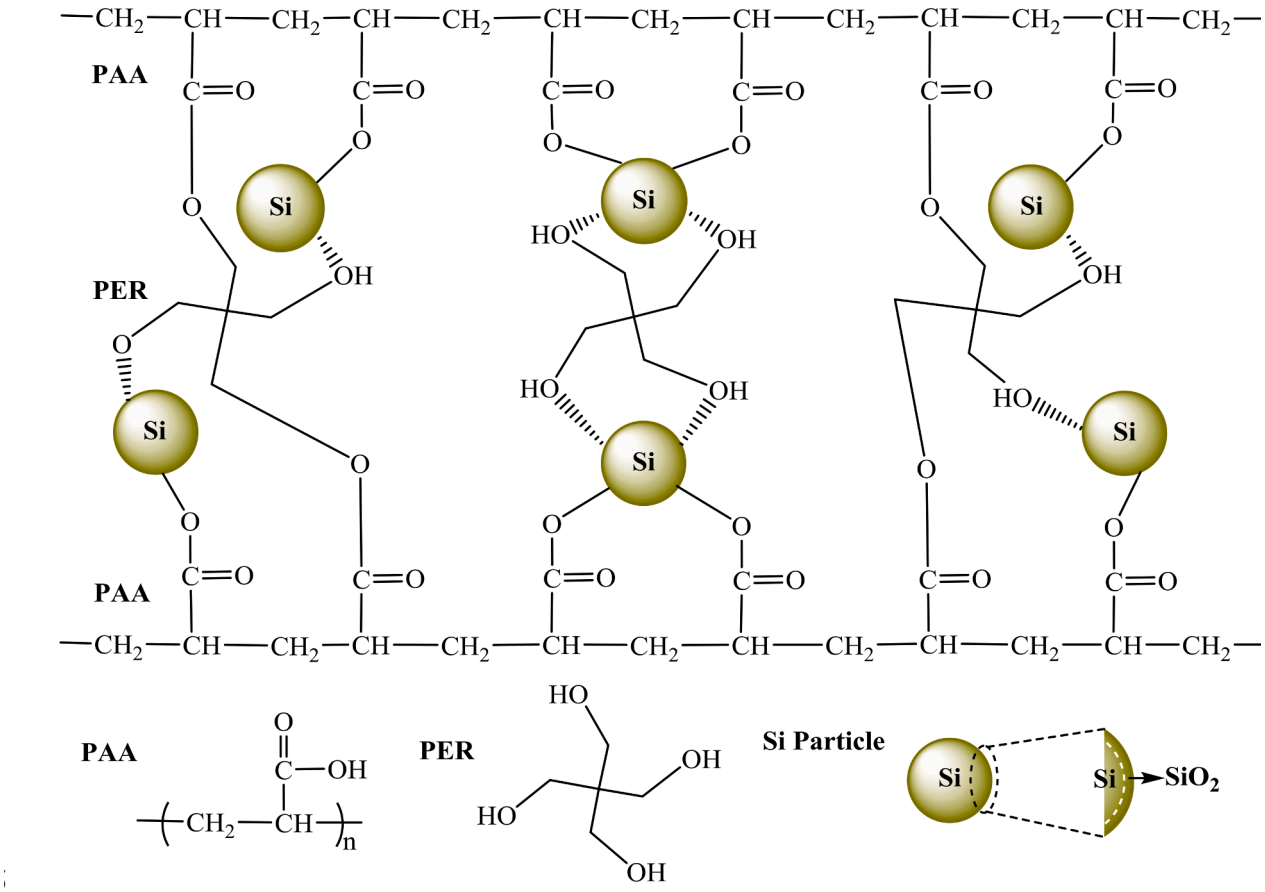

Fig. 1. Schematic illustration of the interactions between crosslinked PAA-PER and Si particles, along with the chemical structure of PAA, PER and Si particle.

the SEI formation on the Si surface can be stabilized by altering the binder type and composition without complicated Si active material synthesis or modification. Moreover, alternative binder designs are more effective, practical and less costly to integrate into application with already-existing battery manufacturing devices.

Recently, many water-soluble binders have been used in Si anodes to improve the electrochemical properties, such as carboxymethyl cellulose (CMC) [13], carboxymethyl chitosan (CCTS) [14, 15], sodium alginate (SA) [16], xanthan gum (XG) [17, 18], guar gum (GG) [19], gum Arabic (GA) [20], cyclodextrin (CD) [21, 22], polyacrylic acid (PAA) [23, 24] and poly (vinyl alcohol) (PVA) [25, 26]. The abundance of functional groups in these polymeric binders such as carboxylic (-COOH) and hydroxylic (-OH) groups can improve the adhesion strength and cycle stability of the Si electrode by forming hydrogen bonding between the -COOH/-OH functional groups and hydrophilic silanol groups (Si-OH) on the Si surface. However, the linear chain nature of these polysaccharide polymer binders makes them susceptible to sliding during continuous volume expansion and contraction in Si electrodes, thus decreasing the stability and integrity of the electrodes during cycling. Therefore, three-dimensional (3D) interconnected networks could enhance the mechanical properties of these linear binders to achieve long-term cycle stability and well-preserved electrode integrity of Si anodes during cycling. Such a 3D interconnected polymeric network can be realized by grafting polymerization and crosslinking reaction. Choi et al. [27] explored a conjugated dopamine on a PAA/SA backbone as an efficient binder for Si anodes to achieve high capacity with improved cycle stability. Koo et al. [28] developed a crosslinked PAA-CMC binder by thermally heating at 150 °C under vacuum for interchain crosslinking and constructed a 3D interconnected network to a achieve high performance Si anode with excellent reversibility. Zhang et al. [29] explored an aqueous crosslinked binder by crosslinking gum Arabic grafted poly (acrylic acid) (GA-g-PAA) and pentaerythrotol (PER)/triethanolamine (TEOA) at 110 °C to construct a robust network for Si anodes with enhanced cycle stability and rate capability. Hong et al. [30] explored a novel dual crosslinked binder synthesized by crosslinking esterification reaction of poly(hydroxyethyl methacrylate) (PHM) and PAA to fabricate Si anodes to obtain good capacity retention. Kim et al. [31] used 1, 6-bismaleimide (BMI) as a crosslinker to furfurylamine-functionalized poly(acrylic acid) (FPAA) and constructed a 3D crosslinked polymer network for Si anodes with self-healing properties. A comparison of 3D grafting and crosslinked polymeric binders is summarized in **Table S1.**, along with the resulting electrode composition, mass loading and electrochemical properties for further comparison. Although many methods can confine the Si particles and maintain the electrode integrity in Si anodes via a 3D interconnected network, the cost of binder preparation, the accessibility of binder materials and their compatibility with the existing manufacturing processes should be considered to enable practical application.

In this work, having manufacture cost and facile preparation routes in mind, we therefore focus on poly (acrylic acid) (PAA) with abundant carboxylic group as a linear framework and pentaerythritol (PER) as a crosslinking agent. The chemical structures of PAA, PER, PAA-PER and their interactions with Si particles are shown schematically in **Fig. 1**, forming a 3D interconnected network between crosslinked PAA-PER binder and Si particles. Firstly, the interactions between PAA and PER are systematically studied and crosslinking is confirmed by Fourier-transform infrared spectroscopy (FT-IR), X-ray photoelectron spectroscopy (XPS) and thermogravimetric (TG) measurements. Secondly, the mechanical and electrochemical properties of Si electrodes with crosslinked PAA-PER binder are evaluated. Finally, surface morphology changes, cross-sectional electrode thickness variations and solid-

electrolyte interphase (SEI) composition of Si-PAA and Si-PAA-5%PER electrodes were analyzed and compared in detail by scanning electron microscopy (SEM), energy-dispersive X-ray analysis (EDX) and XPS measurements. This work provides meaningful insight into exploring facile, interconnected binders and their impact on the SEI formation and functionality, especially for high-capacity alloy-type anode materials.

2. Experimental

2.1. Chemicals

Micro-Si particles (~100 mesh, 99.9%) and nano-Si particles (Diameter: ≤50 nm, 98%, S.A. 70–100 m^2/g, laser synthesized from vapor phase) were purchased from Alfa Aesar. Poly (acrylic acid) (PAA, average Mv ~450 000) was purchased from Sigma-Aldrich. Pentaerythritol (PER, Assay: ≥98%) was purchased from EMD Millipore. Carbon black from Timcal Ltd. was chosen as conducting agent for Si electrodes. All the reagents were used as received. Deionized water (DI-water) was used during the slurry preparation process.

2.2. Materials characterization

2.2.1. Ex situ synchrotron radiation diffraction (SRD)

The crystal structure of the nano-Si particles was measured at the high-resolution P02.1 powder diffraction beamline, storage ring PETRA-III at Deutsches Elektronensynchrotron (DESY) in Hamburg, Germany. The measurements were performed with synchrotron radiation with an energy of 60 keV and a sample exposure time of 60 s. The diffraction patterns at the P02.1 beamline were collected using a two-dimensional (2D) flat panel detector (Perkin-Elmer amorphous Silicon detector) with a sample-to-detector distance of 1600 mm. The resulting 2D images were integrated to one-dimensional diffraction patterns using a X-ray image processing program (Fit2D). The lattice structure parameters and phase fractions were refined using the Rietveld method in the program *FullProf*.

2.2.2. SEM-EDX

The surface morphologies and cross-section thickness of the Si electrodes were obtained by scanning electron microscopy (SEM, Zeiss Merlin) using an acceleration voltage of 10 keV. The coupled energy-dispersive X-ray analysis (EDX) was carried out at a Quantax 400 system (Bruker).

2.2.3. TG

Thermogravimetric measurements (TG) were carried out using a STA 449C Netzsch thermal analyzer with a heating rate of 5 °C min^{-1} up to 800 °C in Ar atmosphere.

2.2.4. XPS

X-ray photoelectron spectroscopy (XPS) measurements were carried out with a K-Alpha XP Spectrometer (ThermoFisher Scientific, East Grinstead, U.K.). Data acquisition and further processing were performed with the Thermo Avantage software, as described by K. L. Parry et al. [32]. All samples were measured with a micro-focused, monochromatic Al Kα X-ray source (1486.6 eV) with 400 μm spot size. The K-Alpha charge compensation system was used for PAA, PER and PAA-5%PER binders during the measurement with electrons of 8 eV energy and low-energy argon ions to prevent localized charge accumulation. The Si electrodes after the 1st and 5th cycle in the charged state were removed from the half-cell. In order to maintain the original state and remove excess electrolyte, the samples were washed with DMC and dried in a glove box. The samples were then transferred under inert gas to the spectrometer using a transfer vessel. The cycled electrodes are measured without the charge compensation system. XP spectra were obtained using a concentric hemispherical analyzer at 50 eV pass energy. The data were fitted with one or more Voigt profiles and Scofield sensitivity factors were used for quantification [33]. All spectra were calibrated in binding energy to the C1s peak (C—C, C—H) at 285.0 eV and the C1s peak (carbon black) at 284.4 eV.

2.2.5. HR-TEM

High-resolution transmission electron microscopy (HR-TEM) was carried out to investigate the Si nanoparticles with a native SiO_2 layer at the atomic scale using a Titan 80–300 electron microscope, equipped with a CEOS image aberration corrector, a high angle annular dark field (HAADF) scanning transmission electron microscopy (STEM) detector and a Tridiem Gatan image filter (GIF). The microscope was operated at an accelerating voltage of 300 kV. The Si samples for TEM measurements were prepared by dispersing the Si nanoparticles into ethanol and then casting on copper grids (Quantifoil Inc.).

2.2.6. Peeling strength experiment

Peeling strength of Si-PAA-1%PER, Si-PAA-5%PER and Si-PAA-10% PER electrodes was quantitatively evaluated by peeling-off experiments using a 3 M tape (adhering to active material side) by a 180° high-precision micromechanical peeling strength tester (Shenzhen Kaiqiangli Corp, China) at constant displacement rate of 20.0 mm min^{-1}, along with a Si-PAA electrode for comparison. The loading used to peel off the active material from the current collector was successively recorded with the displacement. All Si electrodes were pre-dried in vacuum oven

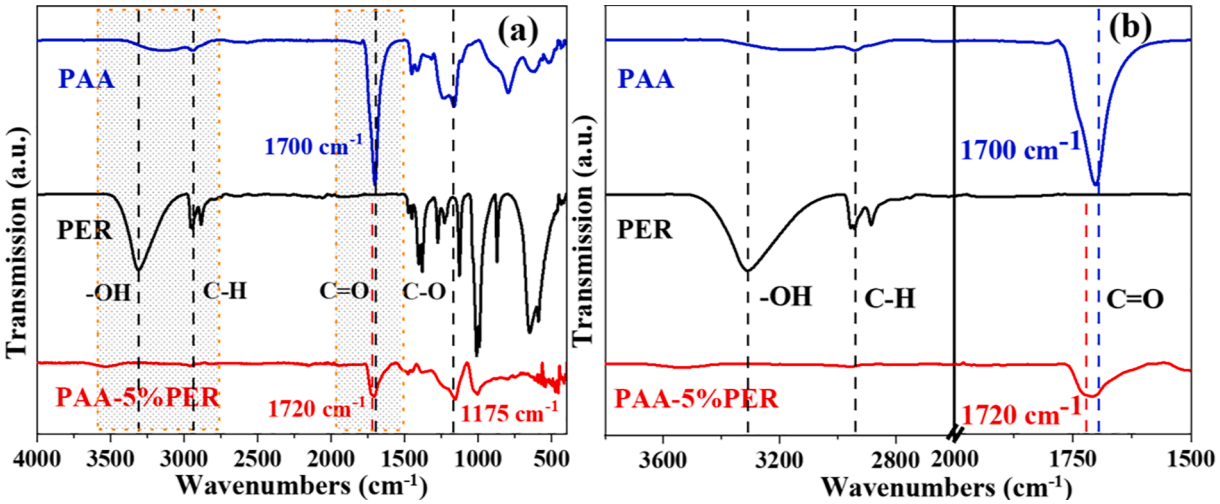

Fig. 2. FT-IR spectra of PAA, PER and PAA-5%PER: (a) Entire spectra; (b) Magnified areas of interested as shaded in (a).

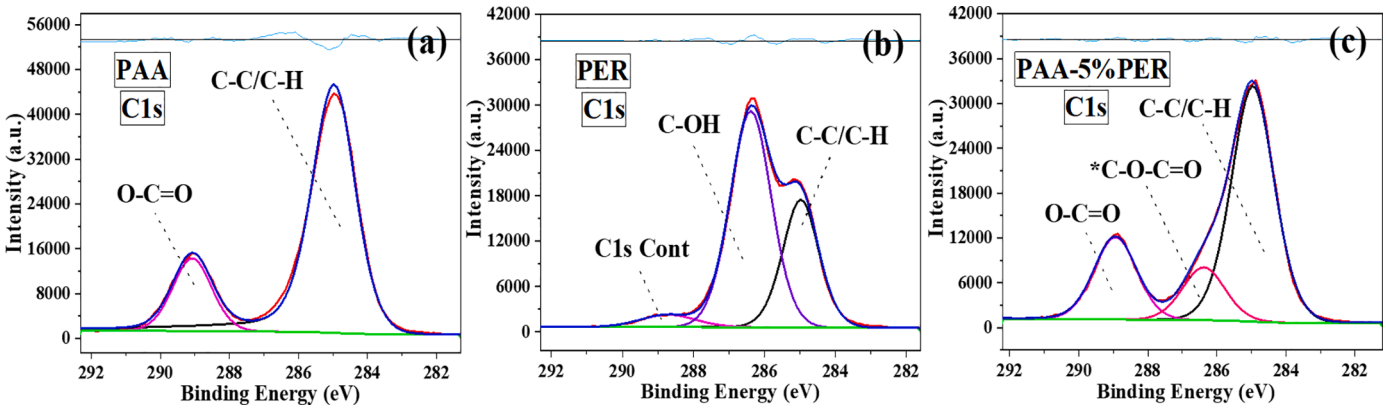

Fig. 3. XPS analysis of the C1s region in PAA, PER and PAA-5%PER binder.

at 70 °C for 24 h before the peeling measurement.

2.3. Electrochemical characterization

A homogenous electrode slurry consisting of Si active material, conducting agent (Super P) and polymeric binders (PAA-PER or PAA) with a weight ratio of 70: 20: 10 was coated on a copper foil by doctor blade to prepare the Si electrodes. The thickness of Si electrodes was controlled to 150 μm during the slurry coating. The crosslinking reaction between PAA and PER in the Si electrodes was activated at 150 °C for 2 h in the oven. The active mass loading of each Si electrode (diameter: 12 mm) was 1.3–2.0 mg cm^{-2}. The electrochemical performances of Si electrodes with PAA and PAA-PER binders were determined using galvanostatic cycling in CR2032 coin-type half-cells. The half-cells were assembled in an argon-filled glove box (MBraun, H_2O, $O_2 \leq 0.1$ ppm) with lithium metal as counter electrode (diameter: 15.6 mm, thickness: 250 μm), 150 μL $LiPF_6$ in ethylene carbonate (EC): dimethyl carbonate (DMC) 1: 1 (V/V) (LP30, BASF) with 10% fluoroethylene carbonate (FEC) additive as electrolyte and one 2325 Celgard membrane as separator, respectively. The coin cells were measured at a current density of 200 mA g^{-1} from 0.01 to 1.50 V (vs. Li/Li^+) at 25 °C in a climate chamber (Binder) during the galvanostatic cycling. All electrochemical measurements including impedance spectroscopy (EIS) were conducted using a Bio-Logic VMP3 multichannel potentiostat. EIS measurements were carried out using an alternating current signal of small amplitude (5 mV) over a frequency range from 1 MHz to 10 mHz.

3. Results and discussion

3.1. Characterization of PAA-PER binder

To investigate the crosslinking reaction between the -COOH groups of PAA and the -OH groups of PER, a portion of PAA polymeric solution was mixed with different amounts of PER (1%, 5%, and 10%, molar ratio to PAA , denoted as PAA-nPER, n = 1%, 5% and 10%), which was then heated at 150 °C for 2 h. Fourier-transform infrared spectroscopy (FT-IR) measurement was used to investigate the crosslinking reaction between PAA and PER after the thermal treatment. As shown in Fig. 2 focussing on PAA-5%PER, the intensity of the broad peak at around 3300 cm^{-1}, which corresponds to the hydroxylic group (-OH) of PER, decreased substantially after the crosslinking reaction. In the meantime, compared to pure PER, PAA-5%PER displayed two new peaks at 1720 cm^{-1} and 1175 cm^{-1}, which correspond to carboxylic ester groups ($-COO^-$) and C—O stretching of the ester moiety, respectively. Moreover, compared to pure PAA, the characteristic peak of the C = O stretching in -COOH shifted from 1700 cm^{-1} to 1720 cm^{-1} in PAA-PER due to the formation of carboxylic ester groups ($-COO^-$) after the crosslinking reaction, whereas the C—H stretching mode at 2943 cm^{-1} remained unchanged. These variations indicate that there are interactions between the -COOH groups of PAA and -OH groups of PER forming carboxylic ester groups ($-COO^-$) via interchain crosslinking under thermal treatment. These interactions form a 3D interconnected polymeric network needed to maintain the Si electrode integrity during volume changes of the Si particles and preserve the electrical contact among Si particles, to conducting agents, and to the current collector.

X-ray photoelectron spectroscopy (XPS) measurements were conducted to further confirm the crosslinking reaction between PAA and PER after the thermal treatment. As shown in Fig. 3, the C1s spectrum of PAA showed characteristic peaks at 285.0 eV and 289.2 eV, which are attributed to C—C/C—H and O—C = O, respectively. In the meantime, the C1s spectrum of PER showed characteristic peaks at 285.0 eV, 286.4 eV and 288.7 eV, which corresponds to C—C/C—H, C—OH and C = O (impurity from the product), respectively. After the thermally induced crosslinking reaction, the C1s spectrum of PAA-5%PER showed characteristic peaks at 285.0 eV, 286.6 eV and 289.1 eV, which are representative of C—C/C—H, *C—O-C = O and O—C = O, respectively. Moreover, the O1s spectra of PAA, PER and PAA-5%PER are shown in **Fig. S1**, which are consistent with the corresponding peaks in C1s spectra. The ester group (*C—O-C = O) present in C1s spectrum of PAA-PER further manifests the crosslinking reaction between PAA and PER under the thermal treatment. Jointly, the XPS and FT-IR results confirm the esterification reaction and the formation of ester groups ($-COO^-$) by crosslinking PAA and PER via the -COOH and -OH groups, respectively, at 150 °C for 2 h.

The crosslinking reaction between PAA and PER was also studied by thermogravimetric measurement (TG) with a heating rate of 5 °C min^{-1} up to 800 °C in Ar atmosphere. As shown in **Fig. S2**, there is some absorbed water evaporation before 100 °C and PAA-5%PER undergoes an extra weight loss at around 150 °C due to the crosslinking reaction. After that, the TG measurement shows thermal stability as no further obvious weight loss happens at least until 200 °C, indicating that both PAA and PAA-5%PER binders are thermally stable in a reasonable temperature range for battery use.

The electrochemical and cycle stability of crosslinked PAA-PER binder was investigated by cyclic voltammetry (CV) measurement, along with PAA binder for comparison. As shown in **Fig. S3**, no obvious oxidative or reductive redox peak can be distinguished from the CV curve of the PAA-1%PER and PAA-5%PER binder film electrodes within the working voltage window, which indicated the electrochemical and cycle stability of the crosslinked PAA-PER binder. The crosslinked PAA-PER binder could therefore provide a robust polymeric network to maintain the electrode integrity and ensure long-term cycle stability for Si electrodes.

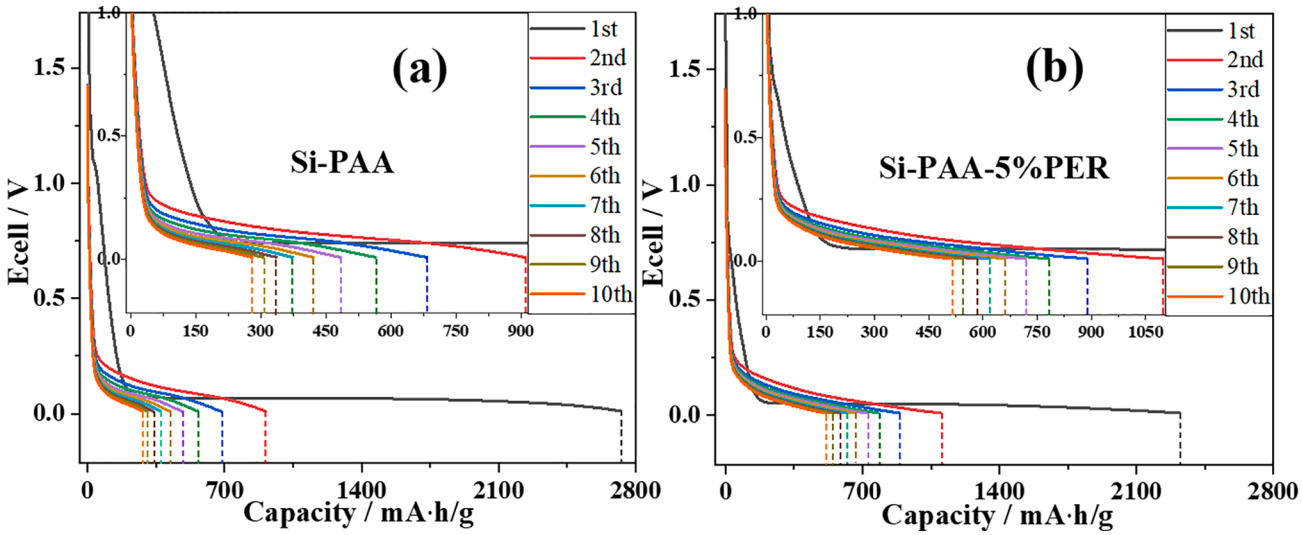

Fig. 4. The discharge voltage profiles for micro-Si electrodes with PAA (a) and PAA-5%PER (b) as binders in the first 10 cycles, the insets are the enlarged areas, respectively.

3.2. Characterization of Si-PAA-PER electrodes

The crosslinking in the PAA-PER binder is also reflected in the mechanical properties of micro-Si electrodes. As shown in **Fig. S4** and **Fig. S5**, the size of micro-Si particles ranges from 1.00 μm to 5.72 μm surrounded by a portion of Si nanoparticles, and its crystal structure belongs to *Fd3_m* space group ($a = b = c = 5.43$ Å, **Table S2.**) without any detectable impurity. The crosslinking was directly incorporated into the electrode fabrication as the coated, wet films were heat-treated at 150 °C for 2 h (more details see **Experimental Section**).

Using either pure PAA or PAA-nPER (n = 1%, 5% and 10%) as binders for micro-Si electrodes, a peeling strength experiment was carried out to quantitatively evaluate the adhesion strength of Si electrodes with different binders. As shown in **Fig. S6** and **Table S3**, the Si-PAA-5% PER electrode possessed a higher peeling strength of 0.48 N cm^{-1} than that of Si-PAA-1%PER (0.37 N cm^{-1}) and Si-PAA-10%PER (0.40 N cm^{-1}), much more superior to that of Si-PAA electrode (0.17 N cm^{-1}). The inferior adhesion of Si-PAA-10%PER may be ascribe to excessive crosslinking in PAA-PER, which decreased the active -COOH sites in the polymeric network and induced detrimental brittleness in the electrode. In addition, folding experiments were further conducted back and forth for 5 times to evaluate the adhesion strength and elasticity of the corresponding electrode coating. As shown in **Fig. S7**, the Si-PAA electrode clearly showed exposed Cu current collector and delamination of the Si active material coating after the folding experiment. Generally, all Si-PAA-PER electrodes maintained their integrity better than the Si-PAA electrode after the folding experiment. Thus, the crosslinked PAA-PER binders enhanced the adhesion strength and elasticity for Si electrodes compared to pure PAA. CV measurements of Si-PAA-nPER (n = 1%, 5% and 10%) and Si-PAA electrodes were also compared and shown in **Fig. S8**. Compared to Si-PAA-1%PER and Si-PAA-10%PER electrodes, Si-PAA-5%PER showed less polarization and higher reversibility during the CV measurement. Among the electrodes with crosslinked PAA-PER binder, which was investigated by peeling strength, folding experiments and CV measurement, the Si-PAA-5%PER electrode possessed the highest adhesion strength, the least cracks/no visible delamination and the best electrochemical reversibility compared to Si-PAA-1%PER and Si-PAA-10%PER electrodes. Therefore, PAA-5%PER was chosen as targeted binder for micro-Si and nano-Si electrodes in the further study and is compared to PAA as a reference.

In this work, micro-Si particles of 1.00–5.72 μm in size with spherical shapes were used as active material to evaluate the effectiveness of PAA-PER binder for micro-Si electrodes. Energy-dispersive X-ray analysis (EDX) was firstly measured to evaluate the main elements and their distribution on the micro-Si, as shown in **Fig. S9**, confirming the presence of a native SiO_x layer (as postulated in Fig. 1) on the surface of micro-Si. The cycle performance was compared by plotting the discharge voltage profiles for a Si-PAA-5%PER electrode and a Si-PAA electrode cycled galvanostatically between 0.01 V and 1.5 V with a current density of 200 mA g^{-1} in a $LiPF_6$/EC-DMC (V/V = 1: 1) electrolyte vs. Li metal as a counter electrode. As shown in Fig. 4, the Si-PAA-5%PER electrode delivered a relatively lower discharge capacity than the Si-PAA electrode in the initial cycle which could indicate lower irreversible capacity losses or less transformation from -COOH to -COOLi during the lithiation process. The Si-PAA-5%PER electrode showed a higher initial columbic efficiency (ICE: 46.7%) and a higher discharge capacity in the 2nd cycle (1098.4 mAh g^{-1}) than the Si-PAA electrode (ICE: 32.6%, 913.3 mAh g^{-1}), which indicated a better passivation layer formed in the Si-PAA-PER electrode. Moreover, the Si-PAA-5%PER electrode maintained a higher discharge capacity of 514.3 mAh g^{-1} after the first 10 cycles compared to the Si-PAA electrode (257.6 mAh g^{-1}). The Si-PAA-5%PER electrode showed an improved cycle stability with decreased capacity fading compared to Si-PAA, which indicates that crosslinked PAA-PER binder can alleviate the internal stress and accommodate the large volume changes of Si particles to a certain extent.

Surface and cross-sectional SEM analyses were conducted to compare the morphologies and thickness variations before and after cycling. As shown in Fig. 5, the Si-PAA-5%PER electrode showed a homogenous distribution of Si active material and conducting agent across the electrode before cycling without obvious differences to the Si-PAA electrode. However, after cycling, the Si-PAA electrode displayed severe pulverization and agglomeration between Si particles and conducting agent while the Si-PAA-5%PER electrode still maintained a distinguishable morphology of individual Si particles and conducting agent without severe aggregation between them. Moreover, the thickness increase of the Si-PAA-5%PER electrode after the first 10 cycles was 114.2% and as such smaller than that of the Si-PAA electrode (134.1%), indicating an enhanced electrode stability and structural integrity due to the strong mechanical properties of the 3D interconnected PAA-PER binder network. The alleviated capacity fading and the improved electrode integrity of the micro-Si-PAA-5%PER electrode showed that crosslinked PAA-PER binder can effectively suppress the pulverization and aggregation of micro-Si particles, accommodating the large volume change of Si particles and restraining the PAA binder from sliding during cycling.

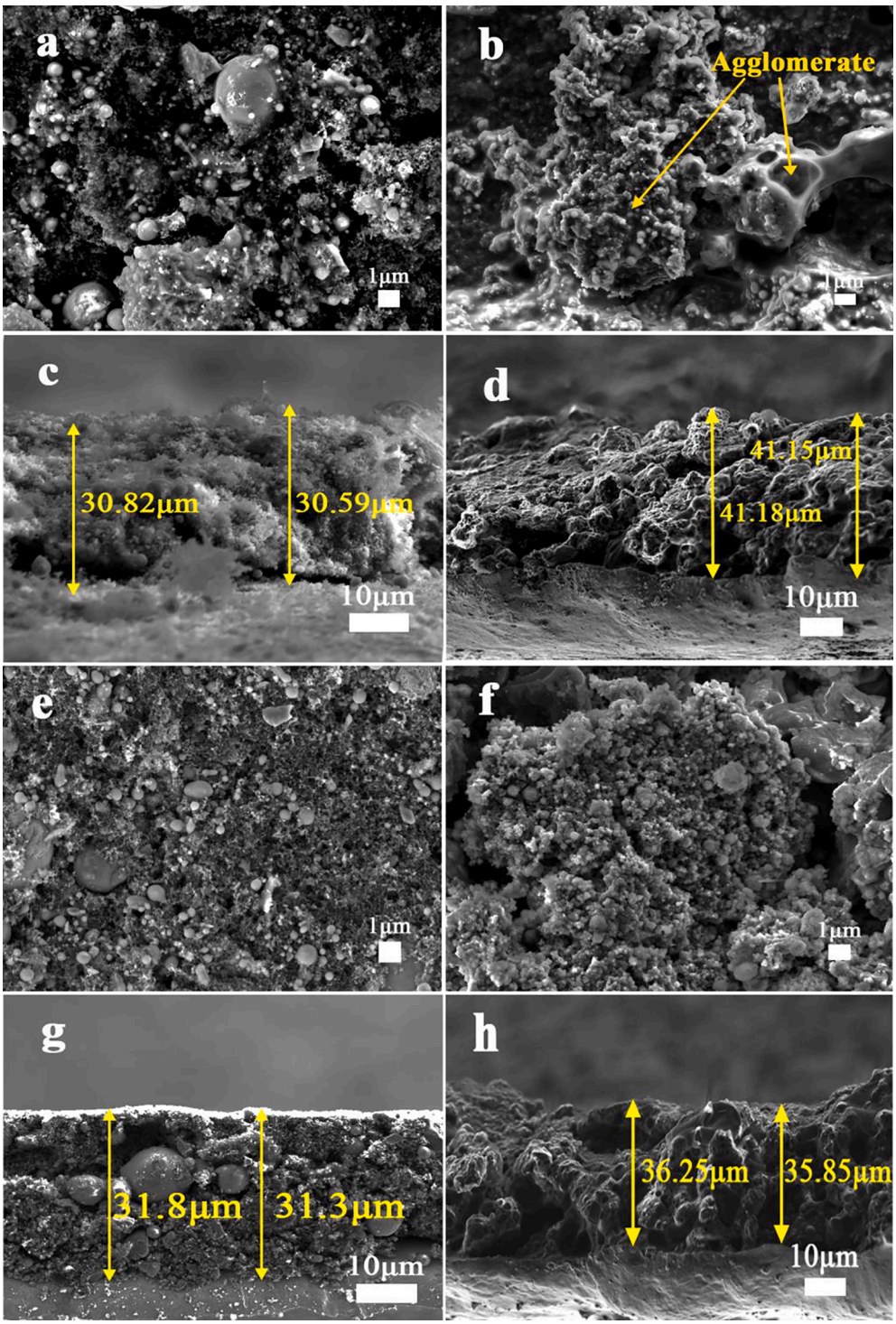

Fig. 5. Surface and cross-section SEM of micro-Si electrodes with PAA (a-d) and PAA-5%PER (e-h) binders before and after the first 10 cycles: (a, c, e, g) before cycling; (b, d, f, h) after cycling.

To test long-term stability, the crosslinked PAA-PER binder is used together with nano-Si particles as active material in Si electrodes. As shown in Fig. 6, the crystal structure of nano-Si particles belongs also to *Fd*3_*m* space group ($a = b = c = 5.43$ Å) without any impurity and its size ranges from 50 nm to 100 nm with spherical shape, as seen from the SEM and TEM images. The native SiO_x layer on the surface of nano-Si particles is confirmed by XPS, as shown in **Fig. S10**. Using PAA-5%PER as binder to prepare nano-Si electrodes with further thermal treatment, the elemental composition and the homogeneity were investigated with EDX and compared to that of Si-PAA electrodes. As shown in **Figs. S11–12**, Si-PAA-5%PER showed a relatively more homogeneous element distribution, especially for C, than that of the Si-PAA electrode, indicating that the PAA-PER binder can improve the homogeneity and dispersion of Si nanoparticles and conducting agent during the slurry preparation process to a certain extent.

Galvanostatic cycling between 0.01 V and 1.5 V with a current density of 200 mA g^{-1} for 105 cycles was conducted to compare the long-term cycling stability of Si-PAA-5%PER electrodes and Si-PAA

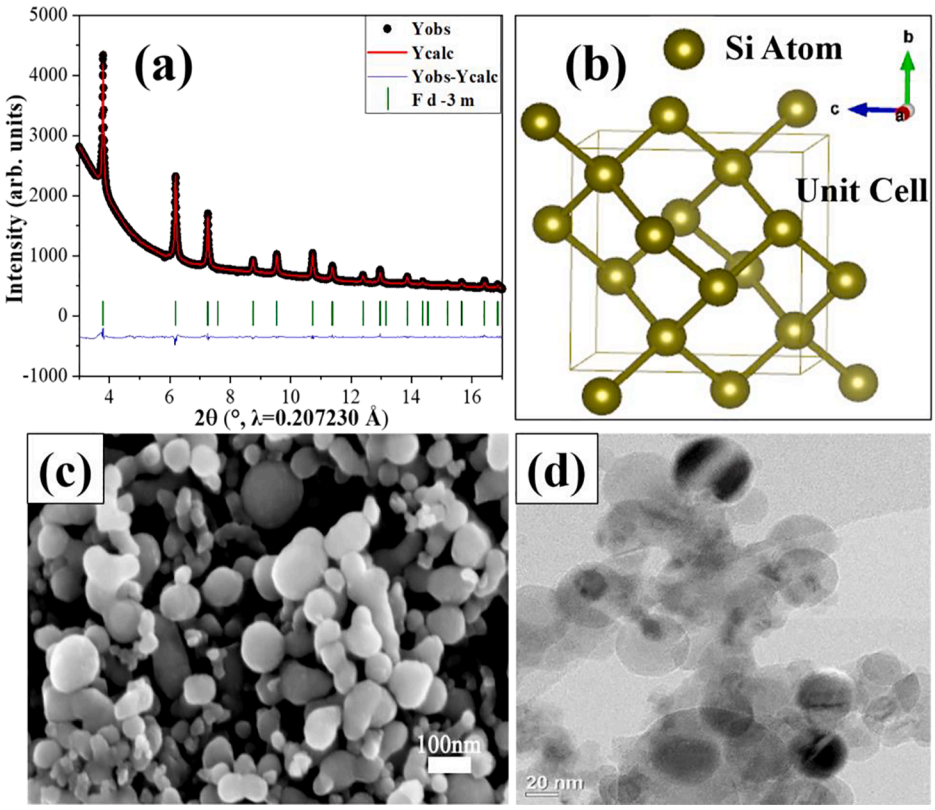

Fig. 6. (a) Rietveld refinement on synchrotron radiation diffraction (SRD) patterns of nano-Si; (b) unit cell and crystal structure of Si with *Fd*3_*m* space group; (c) SEM image of nano-Si particles with diameters of 50 to 100 nm; (d) TEM image of nano-Si particles without distinguishable SiO_x layer on the surface indicating that the native SiO_x is considerably thin on the surface of Si (<1 nm).

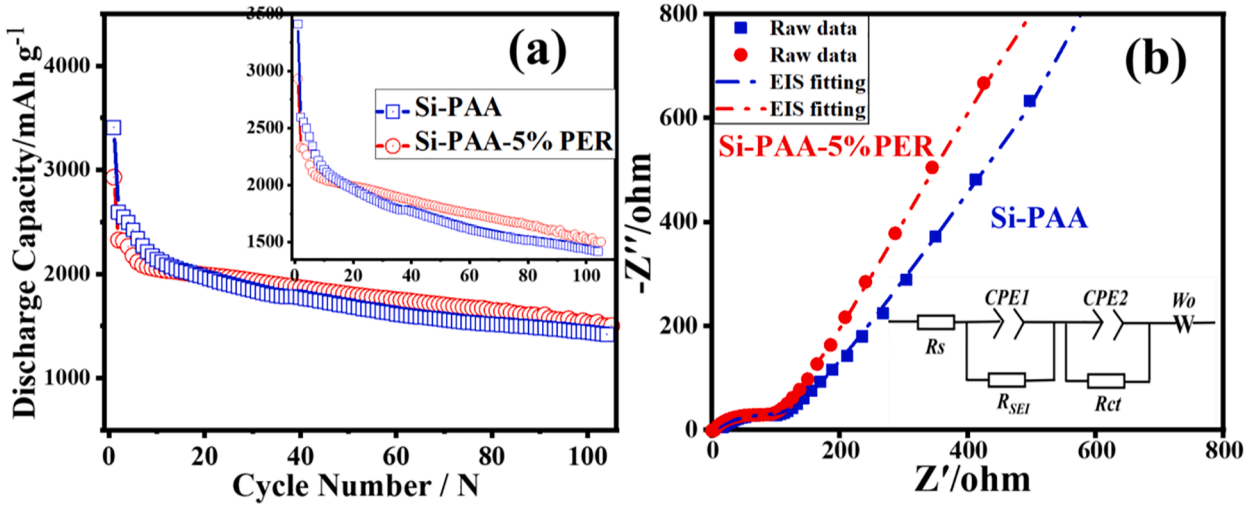

Fig. 7. Cycling performance and electrochemical impedance spectroscopy (EIS) of a Si-PAA-5%PER electrode (red) and Si-PAA electrode (blue): (a) Cycling performance of Si-PAA-5%PER electrode and Si-PAA electrode after 105 cycles at a current density of 200 mA g^{-1}, the inset is the enlarged figure for comparison; (b) EIS curve comparison of the Si-PAA-5%PER and Si-PAA electrodes after 105 cycles at charged state, the inset is the equivalent circuit for fitting EIS raw data.

electrodes. As shown in Fig. 7**a** and **Fig. S13**, the Si-PAA-5%PER electrode maintained a higher discharge capacity of 1502.1 mAh g^{-1}, a higher initial coulombic efficiency (ICE) of 73.2% and a more superior capacity retention of 51.1% after 105 cycles compared to 1413.9 mAh g^{-1}, 71.7% and 41.6% for the Si-PAA electrode. The obtained electrochemical performances of Si-PAA-5%PER are more superior or at least comparable to the other crosslinked binder systems for Si electrode, such as PAA-PVA and PAA-CMC in **Table S1**. In addition, the rate capability of Si-PAA-5%PER and Si-PAA electrodes was tested to investigate the electrode stability and reversibility during fast charging. As shown in **Fig. S14**, the Si-PAA-5%PER electrode possessed a higher discharge capacity and a much more superior rate capability than the Si-PAA electrode at different C-rates. Moreover, electrochemical impedance spectroscopy (EIS) was carried out to compare the impedance differences between the two electrode compositions after 105 cycles in the charged state. As shown in Fig. 7**b**, both EIS curves showed a depressed semicircle and a sloping line, which represents the solid electrolyte interphase impedance (R_{SEI})/charge transfer impedance (R_{ct}) and

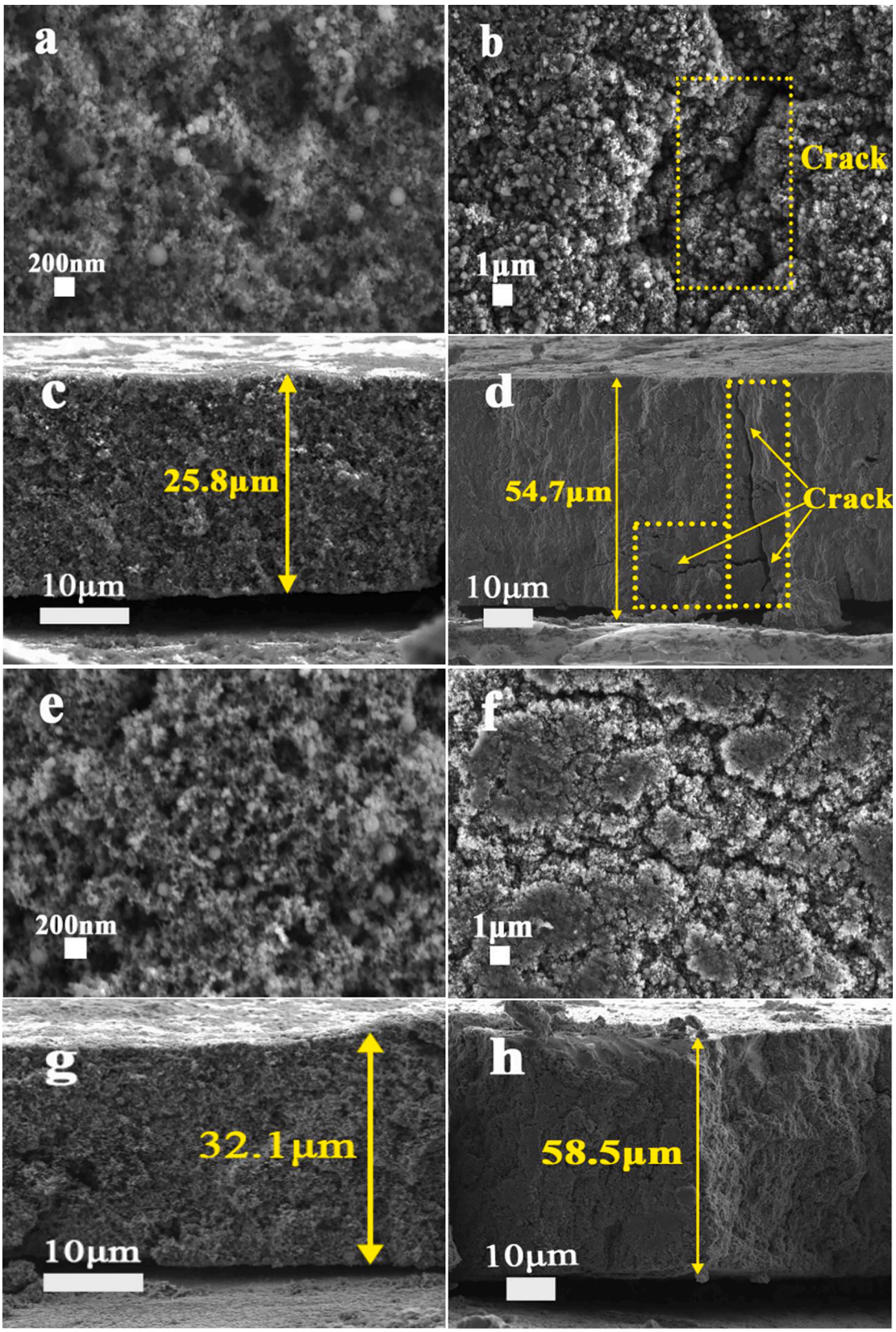

Fig. 8. Surface and cross-section SEM of nano-Si electrodes with PAA (a-d) and PAA-5%PER (e-h) binders before and after 105 cycles: (a, c, e, g) before cycling; (b, d, f, h) after cycling.

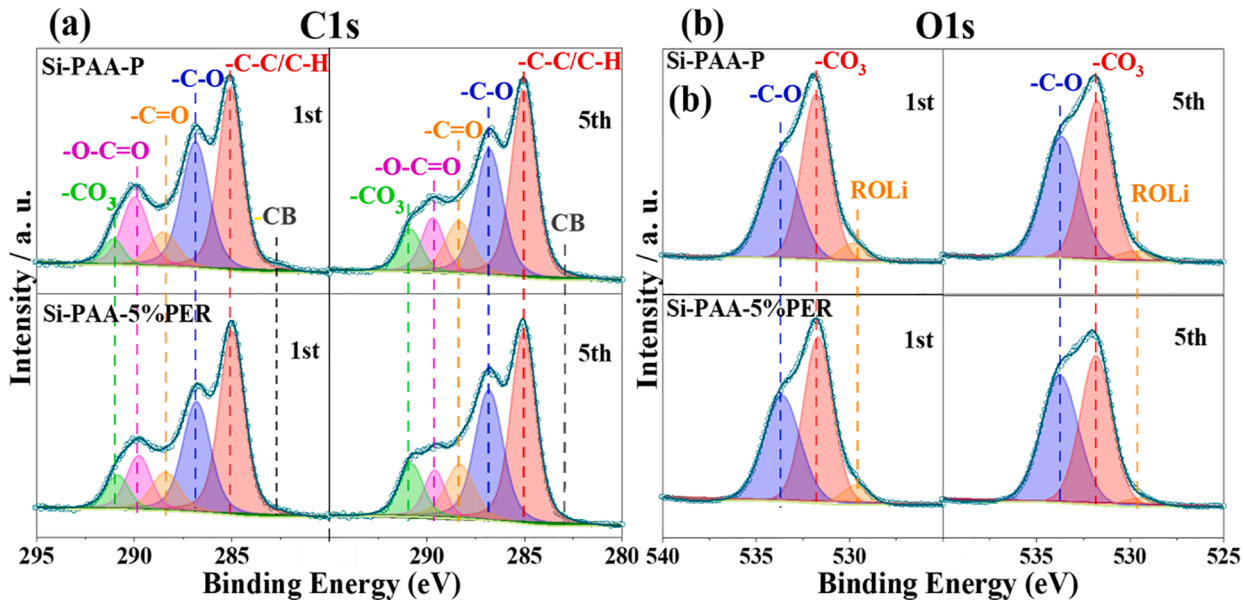

Fig. 9. C1s (a) and O1s (b) XP spectra of the SEI components of Si-PAA and Si-PAA-5%PER electrodes after 1 cycle and 5 cycles at charge state (de-lithiated state).

Warburg impedance (W) in the bulk material, respectively. The inset in Fig. 7**b** is the equivalent circuit for fitting EIS raw data. As displayed in **Table S4**, the Si-PAA-5%PER electrode possessed a lower R_{SEI} impedance (123.9 Ω) and better charge transfer kinetics (R_{ct}, 604.9 Ω) than the Si-PAA electrode (78.2 Ω, 285.1 Ω), characterized by a smaller semicircle in the high-frequency area. The improved cycling performance and enhanced charge transfer kinetics in the Si-PAA-PER electrode point towards the crosslinked PAA-PER binder being able to maintain the intimate contact between the Si active material, the conducting agent and the current collector. By building a 3D interconnected polymeric network within the Si electrode, the PAA-PER binder seems to minimize severe pulverization or agglomeration of Si particles during long-term

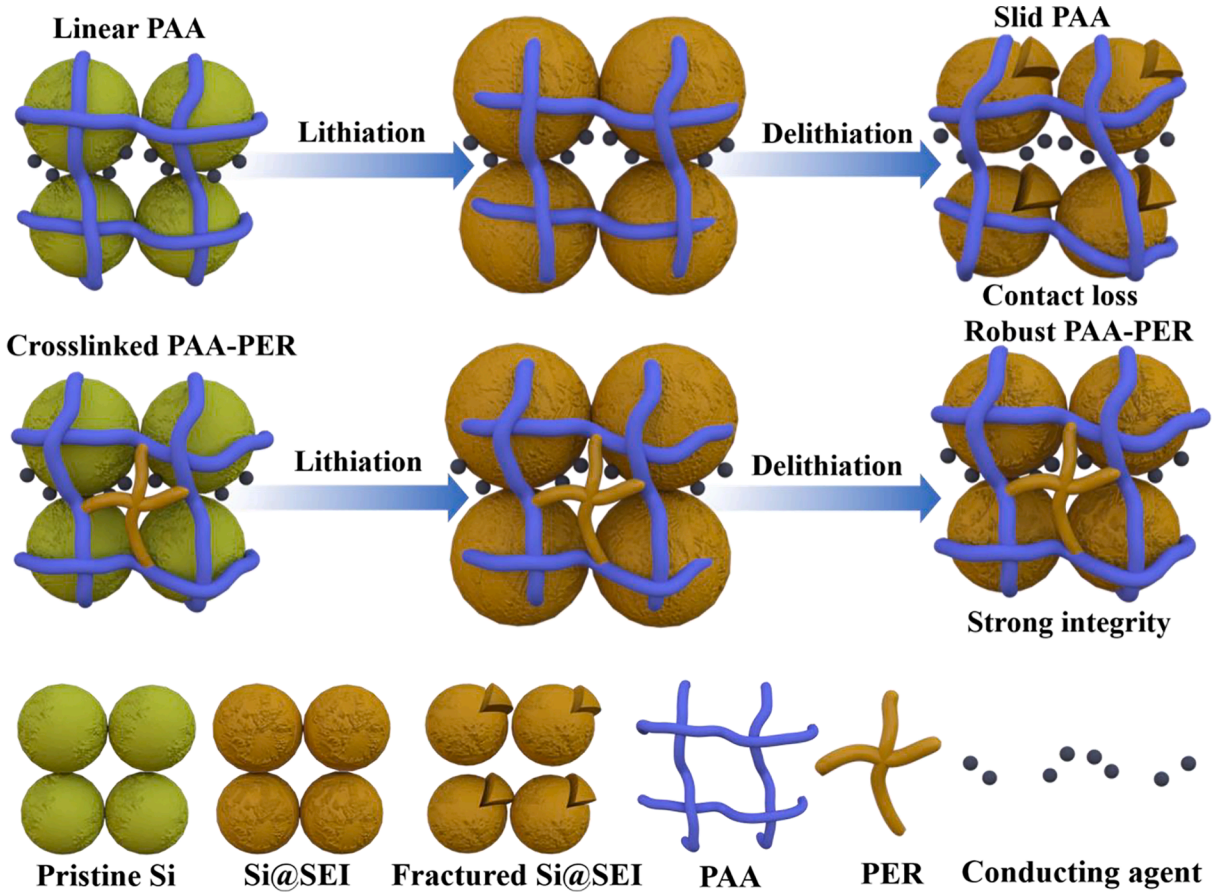

Fig. 10. Schematic illustration and comparison of Si electrodes with crosslinked PAA-PER binder and liner PAA binder during the repetitive lithiation and delithiation of Si particles.

cycling.

In order to further substantiate that a 3D interconnected PAA-PER binder network can maintain the integrity of nano-Si electrodes, surface and cross-sectional SEM was carried out to compare the morphology differences and thickness variations between a Si-PAA-5% PER electrode and a Si-PAA electrode before and after 105 cycles. As shown in Fig. 8, the Si-PAA-5%PER and Si-PAA electrodes showed a homogenous distribution of the Si active material and conducting agent in the electrode before cycling without any obvious difference. However, after long-term cycling, the Si-PAA electrode displayed visible micro-cracks on its surface and in the cross-section due to the induced internal stress from the repetitive volume changes of Si particles during cycling. The micro-cracks were also found in the EDX mapping of the Si-PAA electrode after 105 cycles (**Fig. S15**), which resulted in uneven and inhomogeneous distribution and separation between Si particles and conducting agent. In contrast, the Si-PAA-5%PER electrode maintained its electrode integrity much better, exhibiting mushroom-like isolated islands but with smaller cracks. The elemental distribution in the Si-PAA-5%PER electrode was also more homogeneous than that of Si-PAA electrode, as shown in the EDS mappings in **Fig. S16**. Moreover, the thickness increase of the Si-PAA-5%PER electrode after 105 cycles was 182.2% and thus much smaller than that of the Si-PAA electrode (212.0%), indicating an improved electrode stability and structure.

Combined, the improved electrode integrity, the modest thickness variation and the suppressed crack formation in the Si-PAA-5%PER electrode showed that crosslinked PAA-PER binder can effectively reduce pulverization and aggregation of Si particles. The interconnected network of the crosslinked PAA-PER binder seems to better accommodate the large volume changes of the Si electrode and to restrain the PAA binder from sliding during the long-term cycling.

Since the cycling stability of Si anodes depends mainly on the SEI formation and its functionality, the impact of the PAA-PER and PAA binders on the SEI composition on Si electrodes was further explored and compared in detail. Si-PAA-5%PER and Si-PAA electrodes were firstly cycled for 1 and 5 cycles with current density of 200 mA g^{-1} to form an SEI. The electrodes were analyzed postmortem in the de-lithated state. As the direct comparison of the C1s and O1s XP spectra in Fig. 9 shows, the Si-PAA-5%PER electrode presented almost the same SEI compositions as that of the Si-PAA electrode after 1 cycle. In detail, both SEI layers consisted of organic and inorganic compounds such as C—C/C—H at 285.0 eV binding energy, C—O groups (286.8 eV), C = O groups (288.5 eV), O = C—O groups (289.9 eV) and carbonates (291.0 eV) in the C1s spectrum. The O1s spectrum also showed three peaks of -C-O (533.7 eV), -CO_3 (531.8 eV), and ROLi (529.7 eV) correspondingly [34–37]. After 5 cycles (de-lithiated), the relative intensities of the individual SEI components changed slightly but no obvious difference occurred in either the C1s or O1s XP spectra between the Si-PAA-5%PER and the Si-PAA electrodes. Moreover, as shown in **Fig. S17**, the F1s spectra also showed a similar composition for both electrode types. Since the composition of SEI derived from C1s, O1s and F1s XP spectra did not differ between the Si-PAA-5%PER and Si-PAA electrodes, the improved electrochemical performance is mainly attributed to the superior mechanical properties of PAA-PER and its 3D interconnected network by crosslinking, maintaining good contact among Si particles, conducting agent and current collector.

To visualize the mechanism how the 3D interconnected network of PAA-PER binder maintains the electrode integrity leading to improved electrochemical performance, a schematic illustration and comparison between the Si-PAA-PER electrode and the Si-PAA electrode is presented in Fig. 10. As depicted, before cycling, the two electrodes do not exhibit obvious differences concerning the distribution of Si particles, conducting agent and polymeric binders. After cycling, the Si-PAA-PER electrode preserved an interconnected network and good contact between Si particles and conducting agent, restraining the sliding of linear PAA binder during cycling. In contrast, the Si-PAA electrode cannot maintain the intimate contact between the Si particles and conducting agent, leading to the isolation of fractured Si particles and conducting agent.

4. Conclusion

In summary, a crosslinked PAA-PER binder was prepared via facile thermal treatment of linear PAA polymer with a PER crosslinker, which was systematically studied and manifested by XPS, FT-IR and TG measurements. A 3D interconnected network between Si particles and PAA-PER binder was formed during the crosslinking reaction. The Si-PAA-PER electrode possessed enhanced mechanical properties and robust structure integrity, showing a higher discharge capacity, better cycle stability and superior charge transfer kinetics for micro- and nano-sized Si particles as active material compared to linear PAA binder. Such as, Si-PAA-5%PER electrode with nano-Si possessed a higher discharge capacity of 1502.1 mAh g^{-1}, a higher initial coulombic efficiency (ICE) of 73.2% and a more superior capacity retention of 51.1% after 105 cycles at a current density of 200 mA g^{-1} compared to 1413.9 mAh g^{-1}, 71.7% and 41.6% for the Si-PAA electrode. Cross-sectional SEM showed that crosslinked PAA-PER binder can effectively maintain the electrode integrity and accommodate the large volume change of the Si particles during cycling. XPS results further showed that the PAA-PER binder has no negative impact on the SEI composition and its functionality during cycling compared to using just PAA as a binder. This work provides an experimentally well supported basis into exploring novel binders and their impact on electrode stability and SEI formation, especially for high-capacity alloy-type anode materials.

Credit author statement

J.H. and J.M. oversaw the project; J.H., C.D. and F.Y. carried out the experiments and discussed the results with J.M. The data was analysed by J.H., C.D, F.Y. and J.M. J.H. wrote the preliminary draft, all authors contributed to interpret findings, and review and revise the manuscript.

Supporting Information

XPS analysis of O1s, F1s, Si2p spectra, TG analysis, SEM images, Rietveld refinement results of micro-Si particles, peeling strength test, folding experiment, charge-discharge voltage profile, rate capability, CV measurement, EDX images and Table. S1–4.

Declaration of Competing Interest

The authors declare that they have no known competing financial interests or personal relationships that could have appeared to influence the work reported in this paper.

Acknowledgements

J. H received financial support from the Sino-German (CSC-DAAD) Postdoc Scholarship Program, 2018 (201800260016). C.D. and J.M. are grateful to the German Federal Ministry of Education and Research (FKZ 03XP0131) for financial support. We acknowledge DESY (Hamburg, Germany), a member of the Helmholtz Association HGF, for the provision of experimental facilities. We gratefully acknowledge Alexander Schökel and Martin Etter at beamline P02.1 at PETRA-III for the synchrotron-based diffraction experiments, and Georgian Melinte at institute of nanotechnology (INT, KIT) for TEM measurement. The XPS and TEM characterizations were performed at the Karlsruhe Nano Micro Facility (KNMF), a Helmholtz research infrastructure operated at the KIT. The authors thank Liuda Mereacre for the TG measurements and Udo Geckle (IAM-ESS, KIT) for the SEM experiments. This work contributes to the research performed at CELEST (Center for Electrochemical Energy Storage Ulm-Karlsruhe).

Supplementary materials

Supplementary material associated with this article can be found, in the online version, at doi:10.1016/j.electacta.2022.140038.

References

[1] J.W. Choi, D. Aurbach, Promise and reality of post-lithium-ion batteries with high energy densities, Nat. Rev. Mater. 1 (2016) 16013.
[2] F. Zou, A. Manthiram, A review of the design of advanced binders for high-performance batteries, Adv. Energy Mater. 10 (2020), 2002508.
[3] J.T. Li, Z.Y. Wu, Y.Q. Lu, Y. Zhou, Q.S. Huang, L. Huang, S.G. Sun, Water Soluble Binder, an Electrochemical Performance Booster for Electrode Materials with High Energy Density, Adv. Energy Mater. 7 (2017), 1701185.
[4] J.R. Szczech, S. Jin, Nanostructured silicon for high capacity lithium battery anodes, Energy. Environ. Sci. 4 (2011) 56–72.
[5] C.K. Chan, H. Peng, G. Liu, K. McIlwrath, X.F. Zhang, R.A. Huggins, Y. Cui, High-performance lithium battery anodes using silicon nanowires, Nat. Nanotechnol. 3 (2008) 31–35.
[6] X. Li, M. Gu, S. Hu, R. Kennard, P. Yan, X. Chen, C. Wang, M.J. Sailor, J.G. Zhang, J. Liu, Mesoporous silicon sponge as an anti-pulverization structure for high-performance lithium-ion battery anodes, Nat. Commun. 5 (2014) 4105.
[7] R. Yi, F. Dai, M.L. Gordin, S. Chen, D. Wang, Micro-sized Si-C Composite with Interconnected Nanoscale Building Blocks as High-Performance Anodes for Practical Application in Lithium-Ion Batteries, Adv. Energy Mater. 3 (2013) 295–300.
[8] Y. Yang, Z. Lu, J. Xia, Y. Liu, K. Wang, X. Wang, Crystalline and amorphous carbon double-modified silicon anode: towards large-scale production and superior lithium storage performance, Chem. Eng. Sci. 229 (2021), 116054.
[9] W. Zhang, X. Chen, T. Yong, N. Xu, R. Guan, L. Yue, Multiwalled carbon nanotube webs welded with Si nanoparticles as high-performance anode for lithium-ion batteries, J. Alloys Compd. 688 (2016) 216–224.
[10] H. Tang, J.p. Tu, X.y. Liu, Y.j. Zhang, S. Huang, W.z. Li, X.l. Wang, C.d. Gu, Self-assembly of Si/honeycomb reduced graphene oxide composite film as a binder-free and flexible anode for Li-ion batteries, J. Mater. Chem. A 2 (2014) 5834–5840.
[11] C. Wang, H. Wu, Z. Chen, M.T. McDowell, Y. Cui, Z. Bao, Self-healing chemistry enables the stable operation of silicon microparticle anodes for high-energy lithium-ion batteries, Nat. Chem. 5 (2013) 1042–1048.
[12] X. Yu, H. Yang, H. Meng, Y. Sun, J. Zheng, D. Ma, X. Xu, Three-Dimensional Conductive Gel Network as an Effective Binder for High-Performance Si Electrodes in Lithium-Ion Batteries, ACS Appl. Mater. Interfaces. 7 (2015) 15961–15967.
[13] U.S. Vogl, P.K. Das, A.Z. Weber, M. Winter, R. Kostecki, S.F. Lux, Mechanism of interactions between CMC binder and Si single crystal facets, Langmuir 30 (2014) 10299–10307.
[14] C. Chen, S.H. Lee, M. Cho, J. Kim, Y. Lee, Cross-Linked Chitosan as an Efficient Binder for Si Anode of Li-ion Batteries, ACS Appl. Mater. Interfaces. 8 (2016) 2658–2665.
[15] L. Yue, L. Zhang, H. Zhong, Carboxymethyl chitosan: a new water soluble binder for Si anode of Li-ion batteries, J. Power. Sources 247 (2014) 327–331.
[16] I. Kovalenko, B. Zdyrko, A. Magasinski, B. Hertzberg, Z. Milicev, R. Burtovyy, I. Luzinov, G. Yushin, A major constituent of brown algae for use in high-capacity Li-ion batteries, Science 334 (2011) 75–79.
[17] Z. Wang, Xanthan Gum as a Potential Binder for Graphite Anode in Lithium-Ion Batteries, Int. J. Electrochem. Sci. (2017) 7457–7468.
[18] Y.K. Jeong, T.w. Kwon, I. Lee, T.S. Kim, A. Coskun, J.W. Choi, Millipede-inspired structural design principle for high performance polysaccharide binders in silicon anodes, Energy. Environ. Sci. 8 (2015) 1224–1230.
[19] R. Kuruba, M.K. Datta, K. Damodaran, P.H. Jampani, B. Gattu, P.P. Patel, P. M. Shanthi, S. Damle, P.N. Kumta, Guar gum: structural and electrochemical characterization of natural polymer based binder for silicon-carbon composite rechargeable Li-ion battery anodes, J. Power. Sources. 298 (2015) 331–340.
[20] M. Ling, Y. Xu, H. Zhao, X. Gu, J. Qiu, S. Li, M. Wu, X. Song, C. Yan, G. Liu, S. Zhang, Dual-functional gum arabic binder for silicon anodes in lithium ion batteries, Nano. Energy. 12 (2015) 178–185.
[21] T.w. Kwon, Y.K. Jeong, E. Deniz, S.Y. AlQaradawi, J.W. Choi, A. Coskun, Dynamic cross-linking of polymeric binders based on host-guest interactions for silicon anodes in lithium ion Batteries, ACS Nano 9 (2015) 11317–11324.
[22] T. Kakuta, Y. Takashima, T. Sano, T. Nakamura, Y. Kobayashi, H. Yamaguchi, A. Harada, Adhesion between semihard polymer materials containing cyclodextrin and adamantane based on host-guest interactions, Macromolecules 48 (2015) 732–738.
[23] S. Komaba, T. Ozeki, N. Yabuuchi, K. Shimomura, Polyacrylate as functional binder for silicon and graphite composite electrode in lithium-ion batteries, Electrochemistry 79 (2011) 6–9.
[24] A. Magasinski, B. Zdyrko, I. Kovalenko, B. Hertzberg, R. Burtovyy, C.F. Huebner, T. F. Fuller, I. Luzinov, G. Yushin, Toward efficient binders for Li-ion battery Si-based anodes: polyacrylic acid, ACS Appl. Mater. Interfaces. 2 (2010) 3004–3010.
[25] P. Mandal, K. Stokes, G. Hernández, D. Brandell, J. Mindemark, Influence of binder crystallinity on the performance of Si electrodes with poly(vinyl alcohol) binders, ACS Appl. Energy Mater. 4 (2021) 3008–3016.
[26] S.H. Yook, S.H. Kim, C.H. Park, D.W. Kim, Graphite-silicon alloy composite anodes employing cross-linked poly(vinyl alcohol) binders for high-energy density lithium-ion batteries, RSC Adv 6 (2016) 83126–83134.
[27] M.H. Ryou, J. Kim, I. Lee, S. Kim, Y.K. Jeong, S. Hong, J.H. Ryu, T.S. Kim, J. K. Park, H. Lee, J.W. Choi, Mussel-inspired adhesive binders for high-performance silicon nanoparticle anodes in lithium-ion batteries, Adv. Mater. 25 (2013) 1571–1576.
[28] B. Koo, H. Kim, Y. Cho, K.T. Lee, N.S. Choi, J. Cho, A highly cross-linked polymeric binder for high-performance silicon negative electrodes in lithium ion batteries, Angew. Chem. Int. Ed. 51 (2012) 8762–8767.
[29] H.X. Zhong, J.R. He, L.Z. Zhang, Crosslinkable aqueous binders containing Arabic gum-grafted-poly (acrylic acid) and branched polyols for Si anode of lithium-ion batteries, Polymer 215 (2021), 123377.
[30] M.H. Tsai, J.L. Hong, Dual crosslinked binders based on poly(2-hydroxyethyl methacrylate) and polyacrylic acid for silicon anode in lithium-ion battery, Electrochim. Acta. 359 (2020), 136967.
[31] K.K. R, J. Nam, E. Kim, Y. Kim, T.H. Kim, A self-healable polymer binder for Si anodes based on reversible Diels-Alder chemistry, Electrochim. Acta. 364 (2020), 137311.
[32] A.G.S.K.L. Parry, R.D. Short, R.G. White, J.D. Whittle, A. Wright, ARXPS characterisation of plasma polymerised surface chemical gradients, Surf. Interface. Anal. 38 (2006) 1497–1504.
[33] J.H. Scofield, Hartree-Slater subshell photoionization cross-sections at 1254 and 1487 eV, J. Electron. Spectrosc. Relat. Phenom. 8 (1976) 129–137.
[34] S. Malmgren, K. Ciosek, M. Hahlin, T. Gustafsson, M. Gorgoi, H. Rensmo, K. Edstrom, Comparing anode and cathode electrode/electrolyte interface composition and morphology using soft and hard X-ray photoelectron spectroscopy, Electrochim. Acta. 97 (2013) 23–32.
[35] K. Ciose, k Högström, S. Malmgren, M. Hahlin, M. Gorgoi, L. Nyholm, H. Rensmo, K. Edström, The Buried Carbon/Solid Electrolyte Interphase in Li-ion Batteries Studied by Hard X-ray Photoelectron Spectroscopy, Electrochim. Acta. 138 (2014) 430–436.
[36] G.G. Eshetu, T. Diemant, S. Grugeon, R.J. Behm, S. Laruelle, M. Armand, S. Passerini, In-Depth Interfacial Chemistry and Reactivity Focused Investigation of Lithium-Imide- and Lithium-Imidazole-Based Electrolytes, ACS Appl. Mater. Interfaces. 8 (2016) 16087–16100.
[37] C. Xu, F. Lindgren, B. Philippe, M. Gorgoi, F. Björefors, K. Edström, T. Gustafsson, Improved Performance of the Silicon Anode for Li-Ion Batteries: understanding the Surface Modification Mechanism of Fluoroethylene Carbonate as an Effective Electrolyte Additive, Chem. Mater. 27 (2015) 2591–2599.